Korean J. Chem. Eng., 37(12), 2273-2286 (2020)
DOI: 10.1007/s11814-020-0651-x

pISSN: 0256-1115
eISSN: 1975-7220

Adsorption of copper ions from aqueous media using montmorillonite-Al_2O_3 nano-adsorbent incorporated with Fe_3O_4 for facile separation

Fatemeh Saadat, Mohammad Mahdi Zerafat†, and Sahar Foorginezhad

Faculty of Advanced Technologies, Nano-Chemical Engineering Department, Shiraz University, Shiraz, Iran, 7194684560
(*Received 13 April 2020 • Revised 1 August 2020 • Accepted 2 August 2020*)

Abstract−In the present study, the removal of copper as a common pollutant in industrial wastewaters is considered. For this purpose, montmorillonite (MMT) was doped by Al_2O_3 nanoparticles via precipitation technique. For immediate separation upon removal, Fe_3O_4 nanoparticles were incorporated into the as-prepared nanocomposite matrix. The nanocomposite synthesized via co-precipitation is characterized in terms of morphology and structure using SEM, FE-SEM, EDS and XRD analysis techniques. Also, to verify the magnetic property, value stream mapping (VSM) was performed. To achieve the highest removal rate, effect of parameters such as pH, initial pollutant concentration, amount of adsorbent, temperature and contact time were investigated using Design Expert software. According to the results, at the optimal condition (pH=8.3, pollutant concentration=36 ppm and adsorbent content=77 mg), ~99% Cu (II) removal was obtained. Experimental data are well consistent with Langmuir adsorption isotherm which confirms single layer adsorption. To investigate the adsorbent efficiency in continuous cycles, the adsorbent was utilized in five cycles without washing, indicating an acceptable removal percentage without significant plunge.

Keywords: Industrial Wastewaters, Heavy Metal, Montmorillonite, Nanocomposite, Magnetite

INTRODUCTION

Population growth, clean water shortage and the ever-increasing need for fresh water necessitate the reclamation of wastewater resources. Among various wastewaters, industrial outflows have gained a great deal of attention due to containing a significant quantity of contaminants. Among various pollutants such as petroleum, petrochemicals, dyes, sulfur, phosphates, nitrates and heavy metals, heavy metal ions such as Pb(II), Hg(II), Cd(II), Ni(II), Cr(VI), and Cu(II) as the main group of inorganic pollutants contaminating a vast area due to presence in sludge, fertilizers, pesticides, municipal wastes, mine residues, and smelting industries have been considered as prominent pollutants due to high toxicity and lethal effects [1]. A group of heavy metals, such as Cu, Fe, Ni, and Zn are vital for plant growth but toxic to animals and plants at high concentrations above a threshold level [2]. Among these, although Cu (II) is essential in trace quantity for plants, animals, and humans, higher concentrations can be poisonous or even fatal [3].

According to the World Health Organization (WHO) guidelines for drinking-water quality, the maximum allowable concentration for Cu (II) in drinking water is 2 mg/l [4]. So, various techniques including chemical precipitation, solvent exchange, ion exchange, evaporation, liquid-liquid extraction, membrane filtration and electro-dialysis can be used to remove higher Cu concentrations from wastewaters. Production of large amounts of sludge requiring further treatment is the major drawback of conventional techniques [5]. On the other hand, these techniques are not suitable for treatment of low concentrations; thus adsorption is suggested due to its low-cost, quick processing, high efficiency, easy operation, feasibility and effectiveness [6].

Generally, various natural and synthetic adsorbents, including sawdust [7], various hydrogels [8], calcined phosphate [9], graphene and its derivatives [10], coal fly ash [11], carbon aerogel [12], marine algae biomass [13] and nanoparticles such as silica, titania, Fe_2O_3, ZnO and CuO have been widely used for heavy metals removal, most of which are either not economically viable or technically inefficient [14]. Among various natural and synthetic adsorbents widely used for troubleshooting water contamination by heavy metals, clay minerals have gained a great deal of attention due to superior characteristics such as high adsorption capacity, ion exchange, high surface area, layered structure, abundance, and low cost [15].

Clays are hydrous aluminosilicates, including crystalline or amorphous platy or fibrous minerals such as quartz, carbonates, and metal oxides [16]. The structure can be electrically neutral or charged with a certain interlayer spacing. Moreover, clays benefit from high mechanical, chemical, and thermal stability and cation exchange capacity [17]. They are prominent candidates as natural scavengers for various pollutants through both ion exchange and adsorption where the adsorbed pollutants include anions, cations, non-ionic species and polar molecules accumulated and immobilized on clay edges and surfaces through ion exchange, coordination, or ion-dipole interaction [16-18]. Naturally, clays include exchangeable surface cations and anions such as Ca^{2+}, Mg^{2+}, K^{+}, NH_4^{+}, SO_4^{2-}, Cl^{-}, and NO_3^{-} which can be easily exchanged without clay restructuring. Moreover, various techniques such as intercalation and pillaring [16], acid activation [18], and mechano-chemical activation [19] have been used to improve the adsorption properties. Clay intercalation which is defined as the introduction of guest species

†To whom correspondence should be addressed.
E-mail: mmzerafat@shirazu.ac.ir

into clay interlayer spacing [20], can be evaluated through measuring the space enhancement between adjacent layers using XRD technique [16]. Also, clay pillaring with various metal oxides is of striking value due to enhanced thermal stability, high surface, and catalytic activity [16,17]. For instance, Bhattacharyya and Gupta [17,18] utilized modified minerals for Cu (II) and Cd (II) adsorption from aqueous solutions. Jobstmann and Singh fabricated hydroxy-Al interlayered MMT used for Cd (II) treatment. The data followed the Freundlich isotherm and pillared MMT adsorbed fewer Cd compared with the unpillared one at all concentrations which can be attributed to different sorption mechanisms [21]. It is suggested that, the former retained Cd (II) through electrostatic and chemisorption mechanisms, while the latter adsorbed Cd (II) through electrostatic attraction. After five extractions, pillared MMT desorbed more Cd (II) with a higher rate compared with the unpillared one in spite of desorption at the lowest level of adsorbed Cd (II) which was nearly similar for both clay samples. Dukic et al. synthesized a composite of raw MMT-kaolinite-TiO_2 as additive through mechano-chemical activation used for simultaneous removal of Pb (II), Cu (II), Zn (II), and Cd (II) from aqueous solutions. Based on the results, increasing the TiO_2 content up to 20 wt%, led to a striking enhancement of heavy metal adsorption up to 100% at highly acidic conditions, while little influence on adsorption was observed at pH>2 [22].

In another study, Eren et al. synthesized MgO-coated bentonite and used the composite for Cu (II) removal from aqueous solutions. It was illustrated that the adsorption mechanism followed both Langmuir and Freundlich isotherms [23]. According to the Langmuir monolayer capacity, it was concluded that MgO treatment led to increase the number of adsorption sites, consequently increasing the surface charge. 91% Cu (II) adsorption was obtained at pH=6.5. ZnO/MMT nanocomposite was synthesized and used for removal of Pb (II) and Cu (II) ions from aqueous solutions by Sani et al. [5]. Based on the results, addition of ZnO enhanced adsorption through increasing the surface area caused by intercalation. Higher than 90% Cu (II) and Pb (II) removal was obtained using the as-prepared nanocomposite at pH=4, initial concentration of 100 mg/l during 2 hours. Also, surface area was increased from 169.1 (m^2/g) to 267.1 (m^2/g). Also, increasing the surface area and surface to volume ratio can result in the enhancement of removal efficiency in adsorbents.

Various magnetic nanoparticles have been synthesized and utilized for heavy metals removal with several advantages, such as large surface-to-volume ratio, high number of active sites, and no secondary pollutant leading to high adsorption efficiency, high removal rate of contaminants, and immediate adsorbent separation from the solution using an external magnetic field upon adsorption [24, 25]. Magnetic nanoparticles are mostly composed of iron, nickel, cobalt, and their oxides. Among various magnetic particles, iron oxides have received immense attention owing to their magnetic responsiveness and biocompatibility [26,27]. In tandem with this, the most widely used magnetic nanoparticles are iron-based nanoparticles such as nano zero-valent iron (nZVI), Fe_3O_4 and Fe_2O_3. Also, particle size reduction can lead to the emergence of superparamagnetic behavior and absence of hysteresis in the obtained magnetization curve illustrating low agglomeration in the absence of external magnetic field [27].

In the present study, MMT was used as an adsorbent due to its abundance, non-toxicity, and ion exchanging ability, and low cost. Also, in order to increase the adsorption sites, Al_2O_3 nanoparticles were added via intercalation. Fe_3O_4 nanoparticles were incorporated onto the surface for facile magnetic separation. Based on the literature review, it is predicted that decoration of nano-clay with Al_2O_3 can result in the enhancement of Cu (II) adsorption from aqueous solutions, while Fe_3O_4 though adding to adsorption capacity is mainly expected to provide facile magnetic separation.

EXPERIMENTAL

1. Materials and Methods

1-1. Materials

Aluminum Nitrate (Al $(NO_3)_3 \cdot 9H_2O$, 95%), Ammonium Bicarbonate (NH_4HCO_3, 98%), Copper (II) Sulfate Pentahydrate ($CuSO_4 \cdot 5H_2O$), Sodium Chloride (NaCl), Sodium Hydroxide (NaOH), Iron (III) Chloride ($FeCl_3 \cdot 6H_2O$), Iron (II) Chloride ($FeCl_2 \cdot 4H_2O$), ethanol (C_2H_5OH), and acetone (C_3H_6O) were purchased from Merck Co. Nano-clay (MMT) was purchased from Nanosany Co. (Mashhad, Iran). Deionized water was used for the preparation of all solutions. All reagents, were also used as received without further purification.

1-2. Preparation of Na-MMT

MMT as a natural mineral including insoluble layers is swelled with weakly bound cations in the interlayer spacing. In the present study, Na^+ cations were inserted between MMT layers to increase the interlayer distance. Typically, 5 g of MMT is added to 100 ml of a 1 M NaCl aqueous solution and stirred for 24 h at 60 °C, then centrifuged and washed with deionized water. The water used for washing was tested with $AgNO_3$ aqueous solution with 1 M concentration to trace the presence of chloride ions onto the clay surface. In case of AgCl precipitate formation, MMT was subjected to further washing with deionized water. Consequently, Na-MMT was dried at 100 °C [28].

1-3. Synthesis of MMT-Al_2O_3 Nanocomposite

MMT-Al_2O_3 nanocomposite was synthesized based on Parida et al. [29]. Typically, 45 ml of aluminum nitrate (0.04 M) and 45 ml of ammonium bicarbonate (0.076 M) aqueous solutions were prepared through dissolution of precursors in deionized water. 30 ml deionize water was taken in a round-bottom flask and 2 g of Na-MMT was added to the flask followed by stirring and heating to 70 °C for ion exchange. Then, ammonium bicarbonate and aluminum nitrate solutions were added to Na-MMT suspension in the reaction beaker simultaneously in a dropwise manner. Solution pH was adjusted in the 7.5-8.5 range using NaOH (0.1 M) and the mixture was stirred for 3 h at 70 °C to form aluminum hydroxide on the clay surface. Subsequently, the as-prepared precipitates were filtered and dispersed in hot water and finally washed thoroughly using warm water, ethanol, and acetone to remove traces of Na^+ cations and unreacted precursors. Upon drying at room temperature, calcination was performed at 550 °C for 5 h with a 2 °C/min heating rate.

1-4. Synthesis of MMT-Al_2O_3-Fe_3O_4

For the synthesis of MMT-Al_2O_3-Fe_3O_4 nanocomposite, 60 ml

of deionized water was heated to 65 °C for 15 min initially. Then, 1 g of MMT-Al_2O_3 was added to the solution followed by addition of a 0.04 M aluminum nitrate solution and stirring for 5 min. Subsequently, $FeCl_3 \cdot 6H_2O$ and $FeCl_2 \cdot 4H_2O$ (1 : 1 molar ratio) were added to the solution with 1 : 1 molar ratio of Fe : Al and stirred for 2 h. Next, the solution pH was adjusted at 10 by adding NaOH (2 M) in a dropwise manner while the solution turned dark. Temperature declined to 50 °C and the mixture was stirred for another 3 h. The as-prepared nanocomposite was easily separated using a magnet, washed by deionized water and ethanol several times and dried at the room temperature [30].

2. Characterization

The crystalline structure of MMT and the as-prepared nanocomposites was characterized using X-Ray diffraction (XRD) analysis (Panalytical Xpert PRO X-Ray diffractometer (Holland)). Chemical composition and chemical bonds were verified using Fourier transform infra-red spectroscopy (FTIR) (Nicolet Magna 550 spectrometer) and Raman spectroscopy. Morphology and elemental analysis were defined using scanning electron microscopy (SEM) with energy dispersive X-Ray probe (Mira3-Tescan XMU). Magnetic property of the as-prepared nanocomposite was evaluated using a vibrating sample magnetometer (VSM) (LBKFB, Meghnatis Daghigh Kavir Co.). Atomic absorption spectroscopy (AAS) (ICE 3400, Thermo Scientific) was performed to trace the presence of heavy metals in aqueous solution and to define the removal rate.

3. Removal Experiments

Heavy metal removal from aqueous solution was considered through preparation of Cu (II) aqueous solutions with concentrations in the 5-50 ppm and solution pH in the 3-9 ranges. Typically, certain amounts of the as-prepared nanocomposite in the 20-80 mg range were added to each solution and stirred for 2 h at the room temperature. Then, the solution was centrifuged or separated using a magnet. Cu (II) concentration after 2 h adsorption was measured through AAS technique and removal efficiency was investigated using the following equation:

$$\text{Removal efficiency}\ (\%) = \frac{C_0 - C_e}{C_0} \times 100 \quad (1)$$

where, C_0 and C_e are initial and final Cu (II) concentrations in the aqueous solution.

4. Experimental Design and Data Analysis

Cu (II) removal from aqueous solution using MMT-Al_2O_3 nanocomposite was evaluated using Design Expert software through determining the number of experiments and experiments layout. Response surface methodology (RSM) was also adopted to evaluate the removal percentage under various conditions and specifying the optimal choice. The range of each variable was appointed through screening mode and depicted in Table 1. Meanwhile, to decrease the energy consumption, experiments were performed at room temperature. To fit the experimental results to an equation, a second-order (Quadratic) polynomial was utilized [31]:

$$Y = \beta_0 + \Sigma_{i=1}^{n} \beta_i X_i + \Sigma_{i=1}^{n} \beta_{ii} X_i^2 + \Sigma_{i=1}^{n} \Sigma_{j=i+1}^{n} \beta_{ij} X_i X_j + \varepsilon \quad (2)$$

where, Y is the predicted amount, β_0 is constant or intercept, β_i is the linear, β_{ii} is the quadratic, and β_{ij} interaction coefficient. n is the number of factors. X_i and X_j are variable parameters coded values.

Also, arrangement of the experiments using D-optimal design along with RSM is given in Table 2.

The optimal condition defined using Design Expert optimization section was considered for further removal experiments using MMT-Al_2O_3-Fe_3O_4 nanocomposite to evaluate the effect of Fe_3O_4 on adsorption.

Table 1. Experimental independent variables for response surface methodology (RSM)

Variables	Level of variables			
Solution pH	3	5	7	9
Pollutant concentration (ppm)	5	10	30	50
Adsorbent dosage (mg)	20	40	60	80

Table 2. D-optimal arrangement for three independent variables using RSM

No.	Variables		
	Solution pH	Pollutant concentration	Adsorbent dosage
1	7	30	60
2	3	30	60
3	7	30	60
4	9	5	20
5	3	10	20
6	5	50	80
7	9	50	40
8	3	30	60
9	7	50	20
10	3	50	20
11	5	50	80
12	9	5	80
13	7	30	20
14	5	30	40
15	5	30	40
16	3	10	80
17	9	50	40
18	9	30	80
19	7	5	60

RESULTS AND DISCUSSION

1. Characterization of MMT-Al_2O_3 and MMT-Al_2O_3-Fe_3O_4 Nanocomposites

1-1. XRD Analysis

The crystalline structure of MMT, MMT-Al_2O_3 and MMT-Al_2O_3-Fe_3O_4 nanocomposites was evaluated and compared using XRD analysis given in Fig. 1(a)-(c). According to Fig. 1(a), the reflection relative to 002 plane at 2θ=20.36° confirms the MMT presence. Meanwhile, peaks located at 2θ=13.76° are attributed to kaolin (K), while 2θ=27.26° and 28.41° demonstrate the presence of quarts (Q) [32]. Formation of γ-Al_2O_3 nanoparticles on clay substrate is verified in Fig. 1(b). To be more precise, peaks at 2θ=

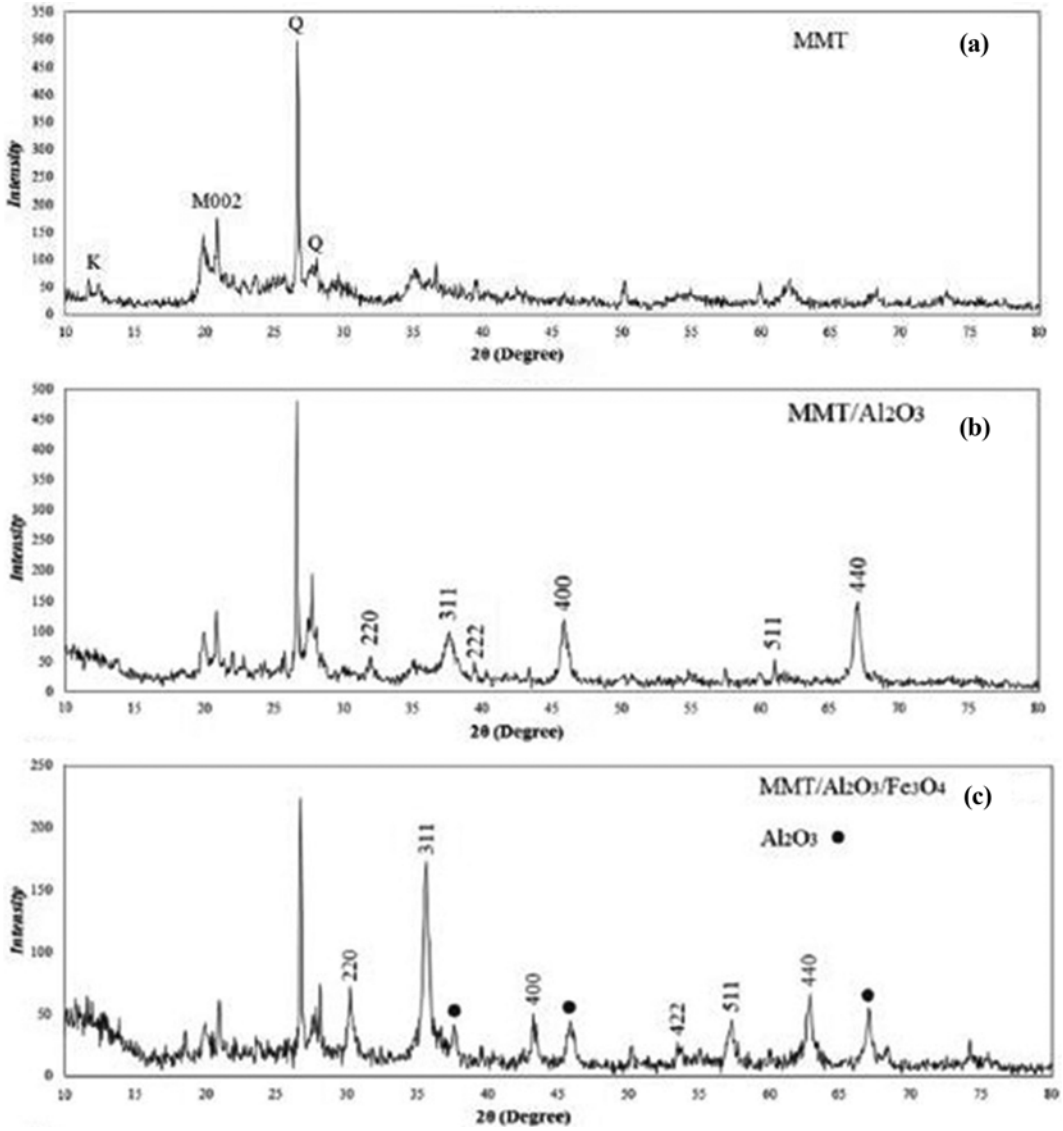

Fig. 1. XRD analysis of (a) MMT, (b) MMT-γ-Al_2O_3, and (c) MMT-Al_2O_3-Fe_3O_4.

31.94°, 37.6°, 39.45°, 45.86°, 61.37°, and 67.03° correspond to (220), (311), (222), (400), (511), respectively and (440) confirms γ-Al_2O_3 formation [33,34]. Incorporation of Fe_3O_4 nanoparticles is also demonstrated using the diffractogram shown in Fig. 1(c). Peaks at 2θ=30.12°, 35.46°, 43.08°, 53.31°, 56.96°, and 62.58° associated with (220), (311), (400), (422), (511), and (440) planes can confirm the formation of Fe_3O_4 on the MMT surface. Although XRD patterns of γ-Al_2O_3 and Fe_3O_4 are generally similar, two extra peaks at 2θ=23.77° and 26.10° related to (210) and (211) planes are attributed to Fe_3O_4 [35].

Incorporation of nanoparticles into the clay structure leads to increase the interlayer spacing that can be evaluated through the peak position in the XRD pattern. In the present study, addition of Al_2O_3 and Fe_3O_4 nanoparticles resulted in increasing the MMT interlayer spacing and shifting the (001) plane, verifying the intercalation state. The peak located at 7.61° shifts toward lower angles and the interlayer distance can be calculated based on the Bragg equation [36]:

$$n\lambda=2d\sin\theta \quad (3)$$

where, n is a positive integer, λ is the wavelength of the incident wave, d is the distance between atomic layers in a crystal, and θ the Bragg's angle (angle of incident). According to Eq. (2), the interlayer spacing of MMT, MMT-Al_2O_3 and MMT-Al_2O_3-Fe_3O_4 is 1.16, 1.4 and 1.6 nm, respectively.

1-2. FTIR and Raman Spectroscopy

Chemical composition and incorporation of Al_2O_3 and Fe_3O_4 nanoparticles to pristine MMT were characterized using FTIR and RAMAN analysis techniques. Figs. 2(a)-(c) depict the FTIR spectra of MMT, MMT/Al_2O_3, and MMT/Al_2O_3/Fe_3O_4, respectively. According to Fig. 2(a), it is illustrated that the appearance of absorption band at 3,620.75 cm^{-1} can be related to the stretching vibration of structural OH groups attached to either Al^{+3} or Mg^{+2} [37]. Also, absorption bands at 778.43, 912.36, 1,000.70, 1,635.91, and 3,403.96 cm^{-1} are assigned to Si-O deformation perpendicular to optical axis, deformation of OH linked to Al^{3+}, Si-O-Si stretching,

H-O-H deformation, and H-O-H hydrogen bonded water, respectively [37,38]. Fig. 2(b) describes the FTIR spectrum of MMT/Al_2O_3. The absorption peak at 1,630.10 cm^{-1} is related to Al-MMT, while the higher intensity (1,635.91 cm^{-1} at Fig. 2(a)) is related to Na-MMT. It is reported this behavior can be related to an improvement in water content in Al-MMT. Also, the absorption peak at 3,426 cm^{-1} with higher intensity compared with Na-MMT (3,403.96 cm^{-1}) can be assigned to O-H stretching vibration in hydroxy-Al cations, while 3,403.96 cm^{-1} is ascribed to hydroxyl groups of water-water hydrogen bonds [39]. Also, the peak at 1,019.43 cm^{-1} corresponds to Al-OH stretching vibration [40] which can overlap Si-O-Si stretching of MMT. Moreover, the band situated at 700.8 cm^{-1} can be related to O-Al-O bond [41]. Fig. 3(c) describes the addition of Fe_3O_4 to MMT/Al_2O_3. It is reported that the formation of Fe_3O_4 can be verified through the absorption peak at 560.43 cm^{-1},

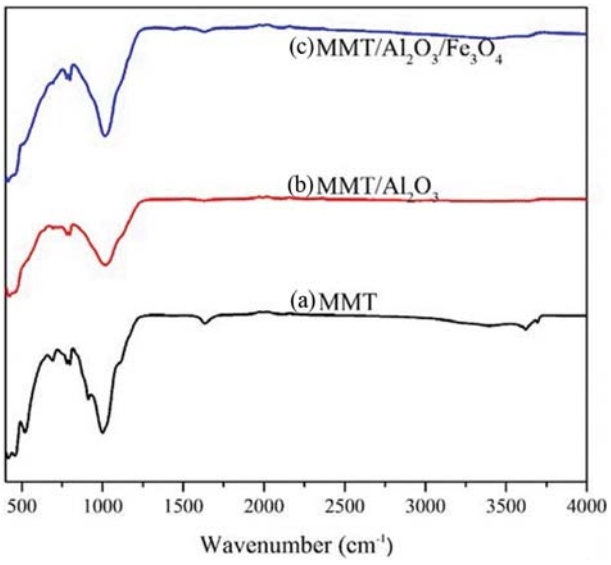

Fig. 2. FTIR spectra of (a) MMT, (b) MMT/Al_2O_3, and (c) MMT/Al_2O_3/Fe_3O_4.

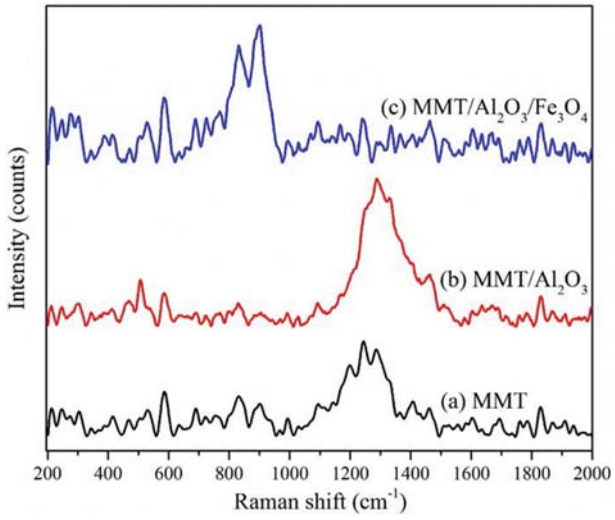

Fig. 3. Raman spectra of (a) MMT, (b) MMT/Al_2O_3, and (c) MMT/Al_2O_3/Fe_3O_4.

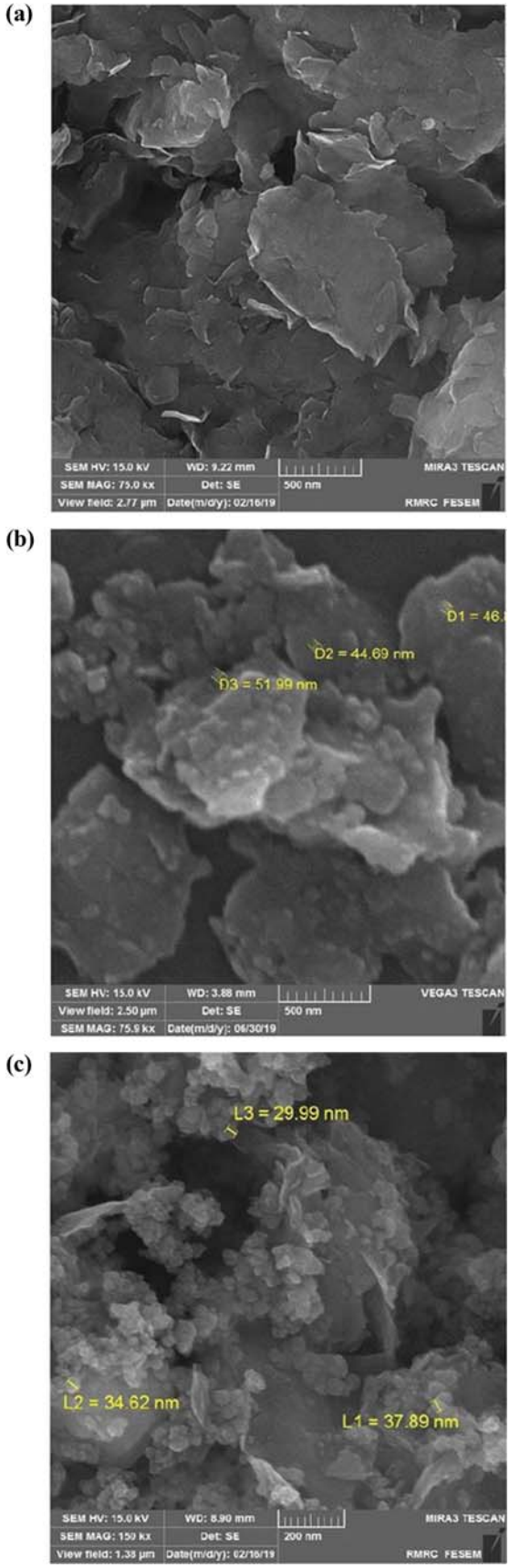

Fig. 4. SEM micrographs of (a) MMT, (b) MMT-γ-Al_2O_3, and (c) MMT-Al_2O_3-Fe_3O_4.

which corresponds to F-O bond [42,43]. Overall, addition of nanoparticles led to decreasing the intensity of pristine MMT characteristic peaks, including Si-O-Si stretching. Also, it can be inferred that nanoparticle characteristic peaks are overlapped with MMT peaks. So, RAMAN spectroscopy was conducted for further clarification.

Raman spectroscopy as a non-destructive method was performed to provide a detailed information about chemical structure and molecular interaction of compounds. Figs. 3(a)-(c) present Raman spectra of MMT, MMT/Al_2O_3, and MMT/Al_2O_3/Fe_3O_4, respectively. According to Fig. 3(a) Raman spectrum of MMT reveals the amorphous structure and low crystallinity along with broad bands. Generally, MMT Raman spectra are characterized by 205.63. 420.14, 715.6 cm^{-1} bands [44]. Precisely, the peak at 715.6 cm^{-1} is attributed to SiO_4 vibration [45]. Moreover, M-OH bending vibrations and Si-O-Si (Al) bending modes correspond to 420.14 cm^{-1} [46]. On the other hand, it is reported that bands in the 600-800 cm^{-1} are assigned to Si-O-Si bonds which connect SiO_4 tertahedra. Also, peaks in the 800-1,150 cm^{-1} can be related to stretching mode of Si-O bond and Al_2O_3 in lattice [45]. Peak at 1,112 cm^{-1} can be attributed to C-H bending mode or C-C bonds in hydrocarbons in organic materials present on clay [45,47]. MMT/Al_2O_3 Raman spectrum is described in Fig. 3(b). Peaks in 550-875 cm^{-1} range correspond to Al_2O_3 formation [48]. Incorporation Fe_3O_4 can be verified through the appearance of peaks at 1,400, 350, 550, and 670 cm^{-1} [49].

1-3. SEM Analysis

Surface morphology of pristine clay and formation of Al_2O_3 and Fe_3O_4 on MMT surface as well as elemental analysis were obtained using FE-SEM micrographs coupled with EDX. Untreated MMT topography with a layered structure can be obviously observed in Fig. 4(a). On the other hand, Fig. 4(b) depicts the formation of Al_2O_3 nanoparticles <60 nm in size on clay surface. Based on Fig. 4(b), separate Al_2O_3 nanoparticles are precipitated on clay surface. Fe_3O_4 nanoparticles with ~35 nm average diameter has also covered the surface at the final step with the surface morphology given in Fig. 4(c). Based on Fig. 4(c), semispherical Fe_3O_4 nanoparticles can be detected distributed homogeneously on the clay surface, resulting in the formation of MMT-Al_2O_3-Fe_3O_4 nanocomposite.

1-4. EDX Analysis

Figs. 5(a)-(c) and Figs. 6(a)-(d) describe the chemical composition using EDX analysis of individual points and map out the distribution of elements from the imaged area. The Al content increases from 10.63 wt% in Fig. 5(a) to 20.53 wt% in Fig. 5(b) via MMT-Al_2O_3 synthesis. Fe_3O_4 content also rose from 2.54 wt% in Fig. 5(a) to 8.29 wt% in Fig. 5(c) due to MMT-Al_2O_3-Fe_3O_4 synthesis. Moreover, EDX maps acquired from initial and modified MMT shown in Figs. 6(a)-(d) depict the presence of Al and Fe content in the MMT matrix.

1-5. VSM Analysis

Magnetic properties of MMT and MMT-Al_2O_3-Fe_3O_4 nanocomposite are demonstrated in Fig. 7 characterized by vibrating sample magnetometer (VSM). Magnetization was reduced from plateau state to zero on removal of the magnetic field. Obviously, MMT exhibits almost no magnetization in the presence of a magnetic field. MMT shows a saturation magnetization (M_s) of 0.057 emu/g, while it enhanced to 30.7 emu/g in case of MMT-Al_2O_3-Fe_3O_4 nanocomposite. No hysteresis loop present in the magnetization curve at the room temperature is consistent with the superparamagnetic property expected for Fe_3O_4 at this size range [50], preventing the agglomeration of nanocomposites upon removal of the magnetic field, which is vital for maintaining removal capacity. The saturation magnetization value observed at the room temperature of 30.7 emu/g is less than its bulk value of 92 emu/g which occurs due to the size effect on magnetization.

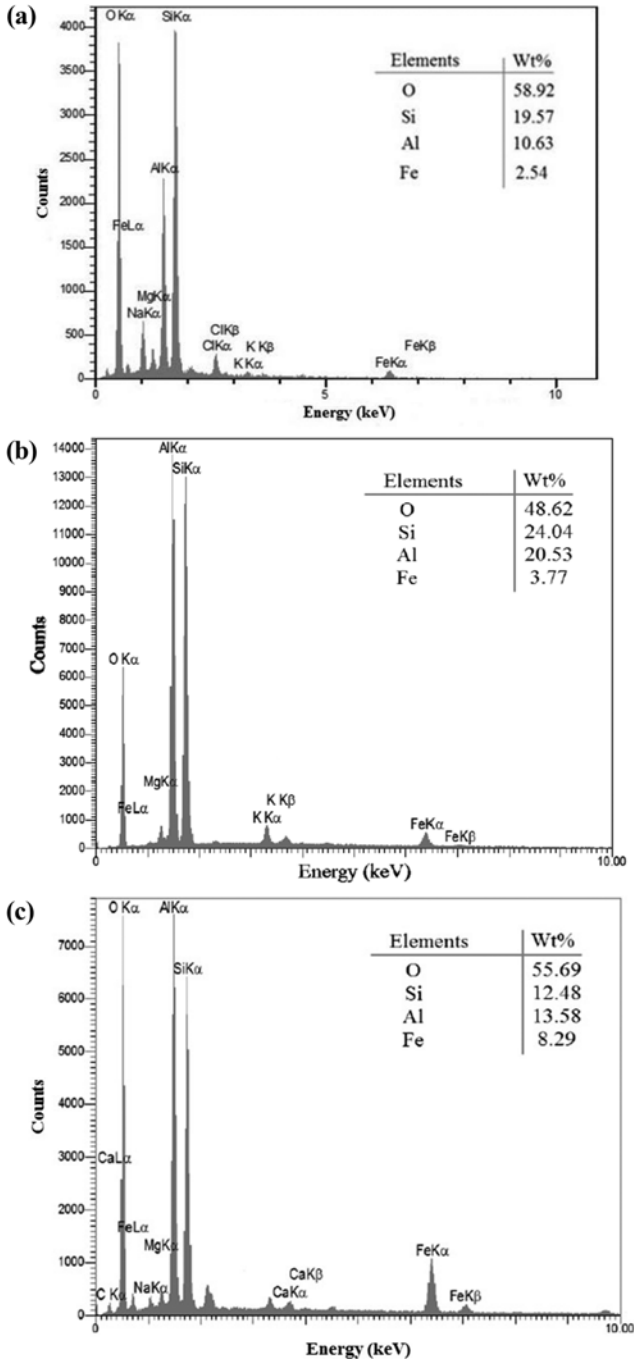

Fig. 5. EDX analysis of (a) MMT, (b) MMT-Al_2O_3, and (c) MMT-Al_2O_3-Fe_3O_4.

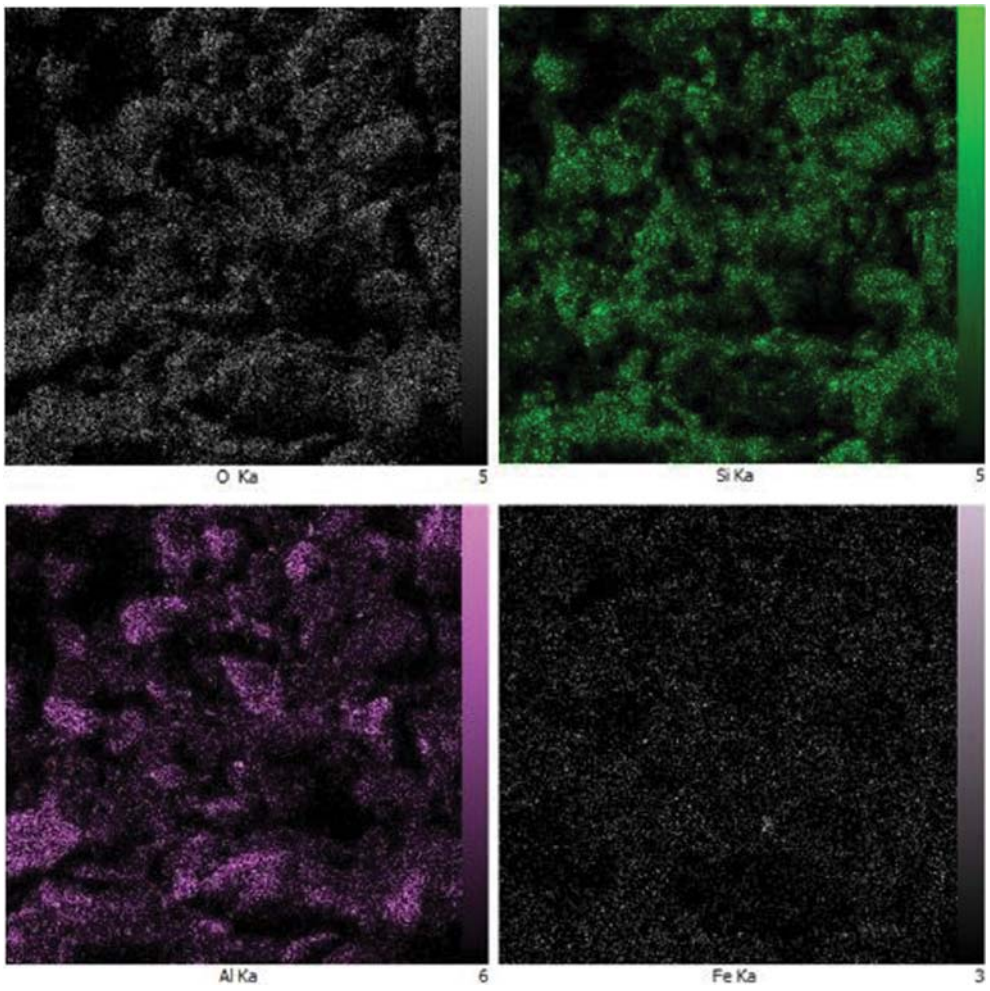

Fig. 6. EDX mapping of MMT-Al_2O_3-Fe_3O_4 in terms of (a) O, (b) Si, (c) Al, and (d) Fe.

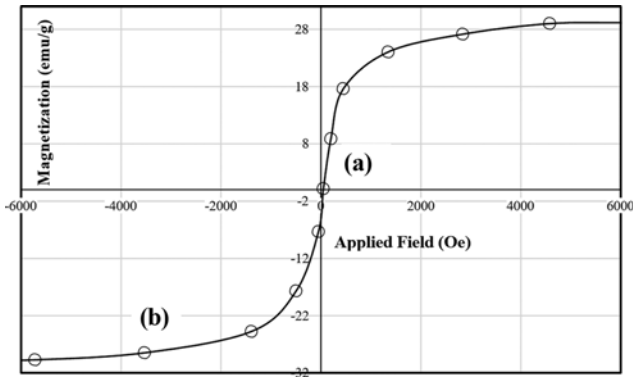

Fig. 7. Magnetization vs. the applied magnetic field for (a) MMT and (b) MMT-Al_2O_3-Fe_3O_4.

According to results obtained from characterization techniques, it can be inferred that alumina and iron nanoparticles were successfully synthesized on MMT surface, while clay crystallinity was retained. Also, addition of Fe_3O_4 particles introduces superparamagnetic properties to clay which results in the ability of the as-prepared nanocomposite being separated using magnetic field without external energy utilization. This property makes the as-prepared nanocomposite a promising candidate for implementation at larger scales.

1-6. PSA and Zeta Potential Tests

Figs. 8(a)-(c) depict the particle size distribution of MMT, MMT/Al_2O_3, and MMT/Al_2O_3/Fe_3O_4. All figures exhibit two separate size distributions; however, most particles are in the nanometer range. MMT particle size distribution is illustrated in Fig. 8(a). Particles are in the 25.7-87.3 nm and 445.1-668.7 nm ranges with a mean value of 58.5 nm. According to Fig. 8(b), incorporation of Al_2O_3 nanoparticles increased the overall size to 29.5-197.1 nm and 388.6-766 nm range and 80.8 nm mean size. Finally, addition of Fe_3O_4 led to particle growth in the 50.7-172.1 nm and 445.1-1,150 nm range with a 187.3 nm mean value (Fig. 8(c)). Overall, 95.71%, 88.36%, and 65.76% of particles are in the nanometer range. It can be inferred that the addition of nanoparticles to the surface enhanced particle size and also improved the surface area which can result in the removal escalation in terms of increased active sites.

Surface charge of MMT/Al_2O_3/Fe_3O_4 nanocomposite in aqueous solutions with various pH was evaluated using zeta potential analysis and the result is in Fig. 9. Based on the results, the high-

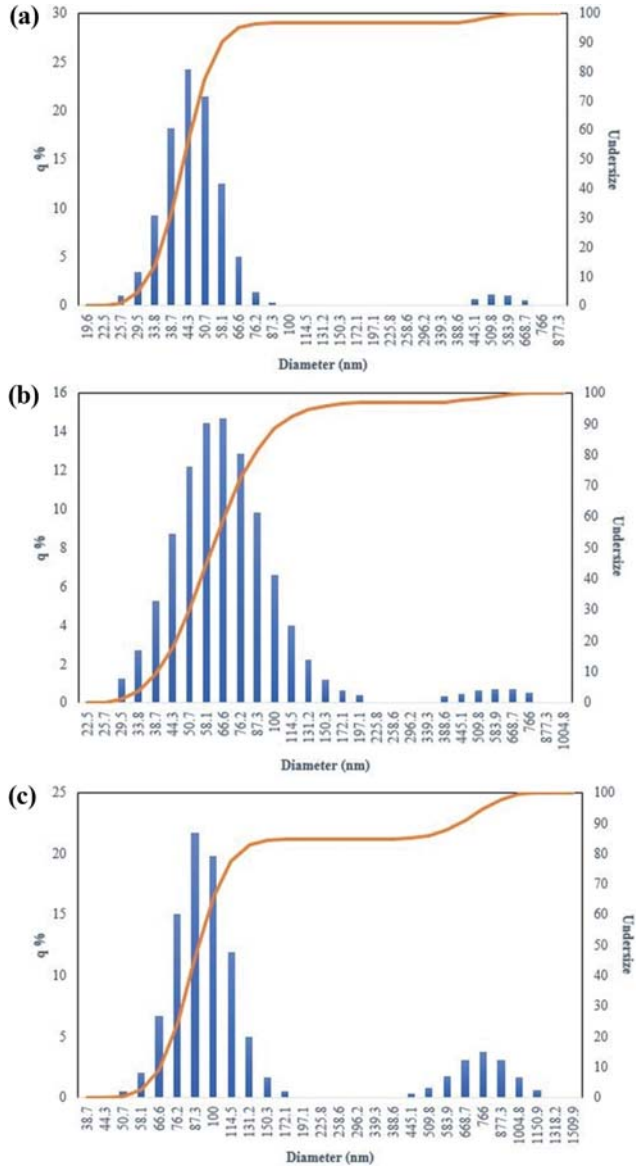

Fig. 8. PSA analysis of (a) MMT, (b) MMT/Al_2O_3, and (c) MMT/Al_2O_3/Fe_3O_4.

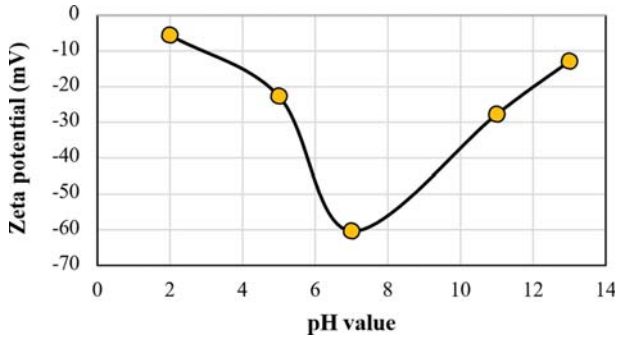

Fig. 9. Zeta potential curve for MMT/Al_2O_3 nanocomposite.

est negative surface charge can be observed around neutral conditions, which is also in accordance with the optimal removal rate at around pH=8.3.

Table 3. D-optimal experiment with actual and predicted values of responses

Run	pH (A)	Pollutant concentration (ppm) (B)	Adsorbent dosage (mg) (C)	Removal (%)	
				Actual value	Predicted value
1	7	30	60	99.15	98.30
2	3	30	60	78.56	80.54
3	7	30	60	99.2	98.30
4	9	5	20	100	99.80
5	3	10	20	77.6	78.03
6	5	50	80	90.91	91.66
7	9	50	40	98.55	99.17
8	3	30	60	81.61	80.54
9	7	50	20	98.73	98.88
10	3	50	20	81.06	80.44
11	5	50	80	91.9	91.66
12	9	5	80	100	100.88
13	7	30	20	97.81	98.21
14	5	30	40	91.11	91.78
15	5	30	40	91.10	91.78
16	3	10	80	82.28	81.82
17	9	50	40	99.43	99.17
18	9	30	80	99.45	98.60
19	7	50	60	100	99.42

2. Data analysis

2-1. RSM Modeling for Cu (II) Adsorption

MMT-Al_2O_3 is used for Cu (II) removal from aqueous solutions. Experiments were designed through RSM technique and the effect of solution pH (A), pollutant concentration (ppm) (B), and adsorbent dosage (mg) (C) were investigated. Other parameters such as temperature, contact time, and alumina dosage in MMT-Al_2O_3 nanocomposite determined using the data from literature and pretests were 28 °C, 120 min, and 0.04 M, respectively. Experimental and predicted values of Cu (II) removal using D-optimal experimental design and RSM technique are summarized in Table 3.

A quadratic equation is successfully fitted to the obtained removal data in order to describe the relation between the variables and responses [51], with an empirical relationship as follows:

$$\%\text{Cu (II) Removal} = 95.85 + 9.6\,A - 0.27\,B + 0.36\,C - 0.6\,AB - 0.79\,AC - 0.97\,BC - 6.08\,A^2 + 0.23\,B^2 - 0.12\,C^2 \quad (4)$$

The influence of each variable and model efficiency was checked by analysis of variance (ANOVA) for the quadratic equation according to Fisher's statistical analysis (Table 4). It was investigated that P-value<0.05 and F-value>0.05 result in a significant variable and play a determining contribution in the model [52]. According to Table 4, the regression model indicated a p-value<0.0001 and F-value of 132.26 illustrates that the model is significant. Moreover, lack of fit p-value and F-value (0.4817 and 1.01, respectively) imply that lack of fit is not significant relative to pure errors. Also, it is clear that the coefficients of pH (A) and its square (A^2)

Table 4. Analysis of variance (ANOVA) for RSM

Source	Sum of squares	Degree of freedom	Mean square	F-value	p-Value>F	
Model	1,195.59	9	132.84	132.26	<0.0001	Significant
A	918.94	1	918.94	914.89	<0.0001	
B	0.62	1	0.62	0.62	0.4525	
C	1.36	1	1.36	1.35	0.2745	
AB	1.94	1	1.94	1.93	0.1981	
AC	3.63	1	3.63	3.62	0.0896	
BC	6.25	1	6.25	6.22	0.0342	
A^2	113.94	1	113.94	113.44	<0.0001	
B^2	0.15	1	0.15	0.15	0.7064	
C^2	0.041	1	0.041	0.041	0.8449	
Residual	9.04	9	1.00			
Lack of fit	4.04	4	1.01	1.01	0.4817	Not significant
Pure error	5.00	5	1.00			
Total error	1,204.63	18				

are highly significant (p-value<0.0001) in comparison with other coefficients. The goodness of fit of the model was evaluated using multiple correlation coefficient (R^2). In this study, R^2=0.9925 reveals that this regression is statistically significant, and higher than 99.25% of the data deviation can be explained by the model. On the other hand, the predicted multiple correlation coefficient value (pred. R^2= 0.9637) is in agreement with the adjusted multiple correlation coefficient value (adj. R^2=0.9850).

2-2. Effect of Solution pH, Cu (II) Concentration, and Adsorbent Dosage on Removal

According to the literature review and empirical results, removal of metal ions from aqueous solutions is strongly dependent on solution pH. Overall, surface charge of clay mineral plays a dominant role in the adsorption process [53]. According to Fig. 10, adsorption of Cu (II) ions onto the adsorption sites would be enhanced by increasing solution pH related to the clay surface charge and a strong competence between H^+ and divalent ions. Precisely, clay surface becomes negatively charged as the pH is increased. So, Cu (II) ions are adsorbed onto the surface due to diminishing the repulsive force. In addition, at pH>7, removal slightly increased and then started to decrease at pH>8.5 which can be attributed to the precipitation of Cu $(OH)_2$ in the solution [53].

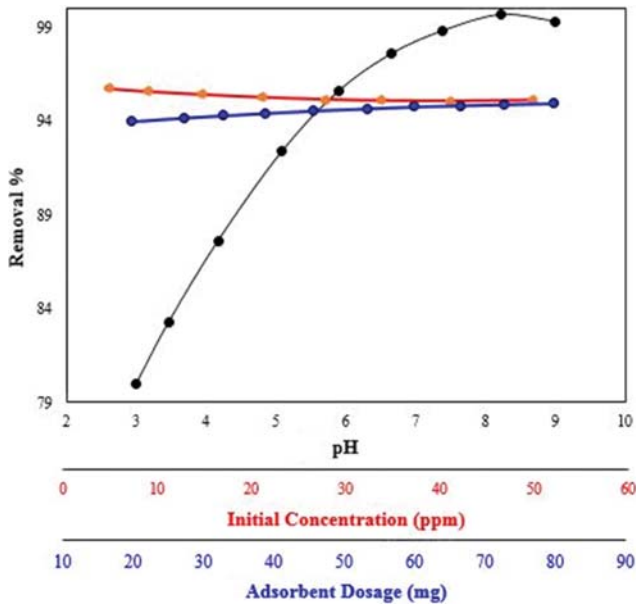

Fig. 10. Effect of pH, initial pollutant concentration, and adsorbent dosage on Cu (II) removal using MMT-Al_2O_3 nanocomposite.

Effect of Cu (II) concentration on removal can be predicted through Fig. 10. It is clear that the removal rate is slightly decreased as the initial pollutant concentration increases up to 50 ppm. This behavior can be attributed to the lack of adsorption sites at high Cu (II) concentration. Fig. 10 indicates the effect of adsorbent dosage on Cu (II) removal. It can be inferred that increasing the adsorbent content leads to a slight removal rate enhancement which can be related to increasing the adsorption sites available for Cu (II) ions. Regarding Fig. 10, solution pH clearly plays a significant role in Cu (II) removal compared to other factors, which is in agreement with p-values in Table 4.

2-3. Interaction of Parameters on Cu (II) Removal

The combined effect of solution pH and initial pollutant concentration is shown in Figs. 11(a) and (b). It can be concluded that increasing the pollutant concentration does not have a significant impact on removal rate, while a striking enhancement is obtained by pH enhancement. On the other hand, Figs. 12(a) and (b) indicate the effect of solution pH and adsorbent dosage on Cu (II) removal. Solution pH obviously plays a dominant role compared to adsorbent dosage and Cu (II) removal rises to >98% at pH>7. The interaction effect of initial pollutant concentration and adsorbent dosage is depicted in Figs. 13(a) and (b). It can be inferred that at low initial concentrations, increasing the adsorption dosage leads to Cu (II) removal enhancement, while this behavior is reversed at high pollutant concentrations. On the other hand, at low adsorbent content, increasing the initial pollutant concentration results in increasing Cu (II) removal and this behavior is reserved at high adsorbent dosages. It is worth noticing that the variations are negligible, which can be related to low Cu (II) concentration and vari-

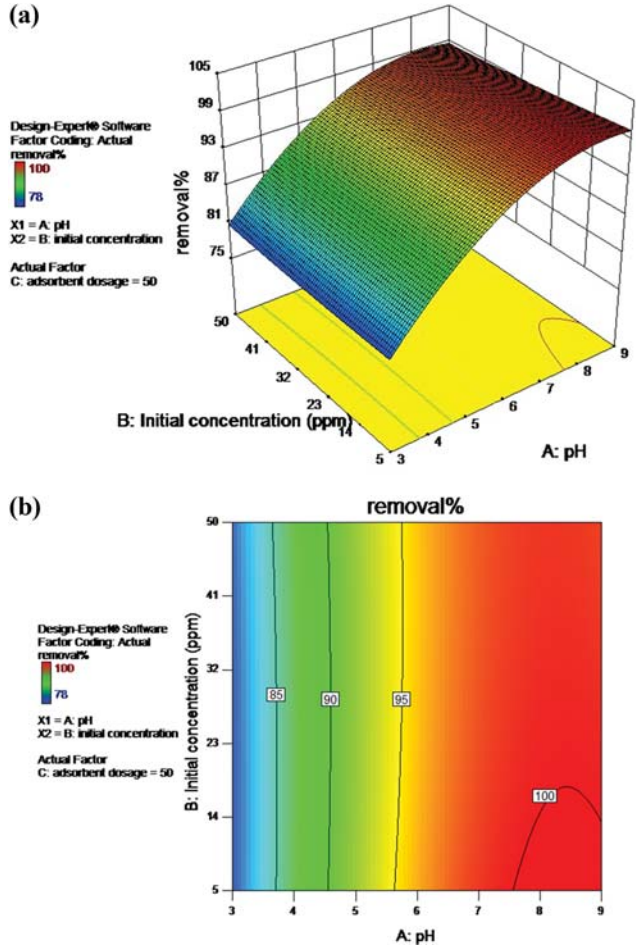

Fig. 11. (a) 3-D response surface plot and (b) contour plot showing the interaction effect of solution pH and initial pollutant concentration on Cu (II) removal using MMT-Al_2O_3 nanocomposite.

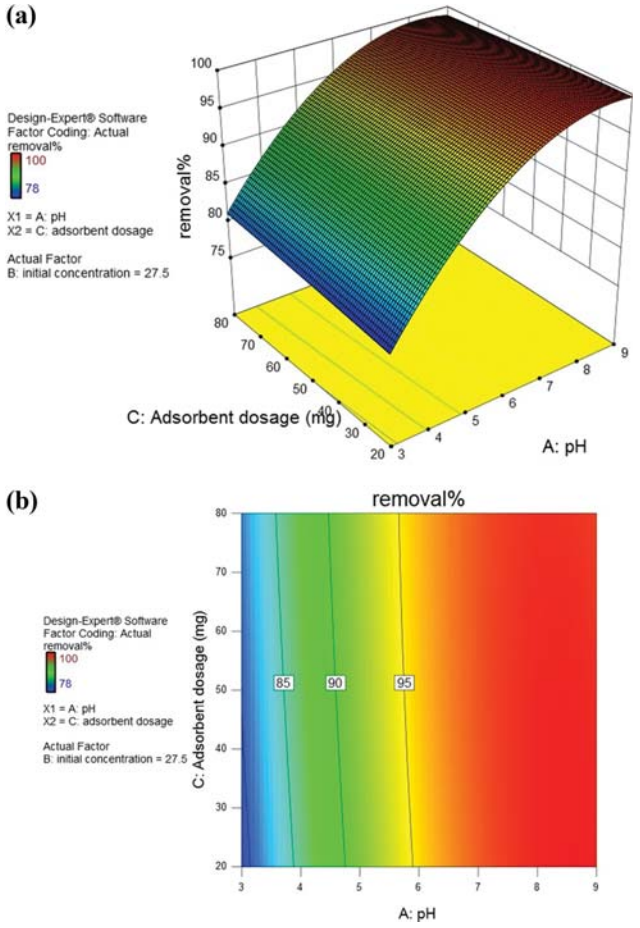

Fig. 12. (a) 3-D response surface plot and (b) contour plot showing the interaction effect of solution pH and adsorbent dosage on Cu (II) removal using MMT-Al_2O_3 nanocomposite.

ation of adsorption capacity at various pollutant concentrations.

Numerical optimization of the model was applied to find the highest Cu (II) removal from aqueous solutions at low adsorbent dosage. According to the optimal conditions generated by numerical optimization section of Design Expert software, it was observed that the optimal condition with % Cu (II) removal=99% occurs at pH=8.3, pollutant concentration=36 ppm, and adsorbent dosage= 77 mg. Also, the results were confirmed by performing several experiments under the optimal condition specified by the software. Repeating experiments at optimal condition resulted in 99.64%, 99.71%, and 98.7% Cu (II) removal rates from aqueous solutions, which confirmed the model accuracy.

3. Adsorption Isotherm for MMT-Al_2O_3

Generally, the adsorption mechanism is described using isotherms of the adsorbed amount vs. the adsorbent content. It is reported that the distribution of metal ions in solution and on solid phase can be described using Langmuir and Freundlich models [54]. A monolayer adsorption onto the surface with finite adsorption sites without transmigration of adsorbate along the plane surface is attributed to the Langmuir isotherm [55]. Langmuir isotherm is described as follows:

$$\frac{C_e}{q_e} = \frac{1}{K_L q_{max}} + \frac{C_e}{q_{max}} \tag{5}$$

where, constant K_L and q_{max} are energy of adsorption and maximum adsorption capacity and C_e and q_e are equilibrium concentration and adsorption capacity, respectively. Also, a dimensionless constant was calculated for this model (R_L) that predicts the practicability of the adsorption process:

$$R_L = \frac{1}{1 + K_L C_i} \tag{6}$$

where, K_L is the Langmuir constant and C_i (mg/L) the minimum initial copper concentration. R_L values smaller than unity mean favorable adsorption.

Freundlich isotherm is described as follows as an empirical model [54]:

$$\log q_e = \log K_f + \frac{1}{n} \log C_e \tag{7}$$

where, K_f and n are adsorption capacity and adsorption intensity, respectively.

In this study, Figs. 14 (a) and (b) reveal a linear plot of specific adsorption (C_e/q_e) as a function of equilibrium concentration (C_e)

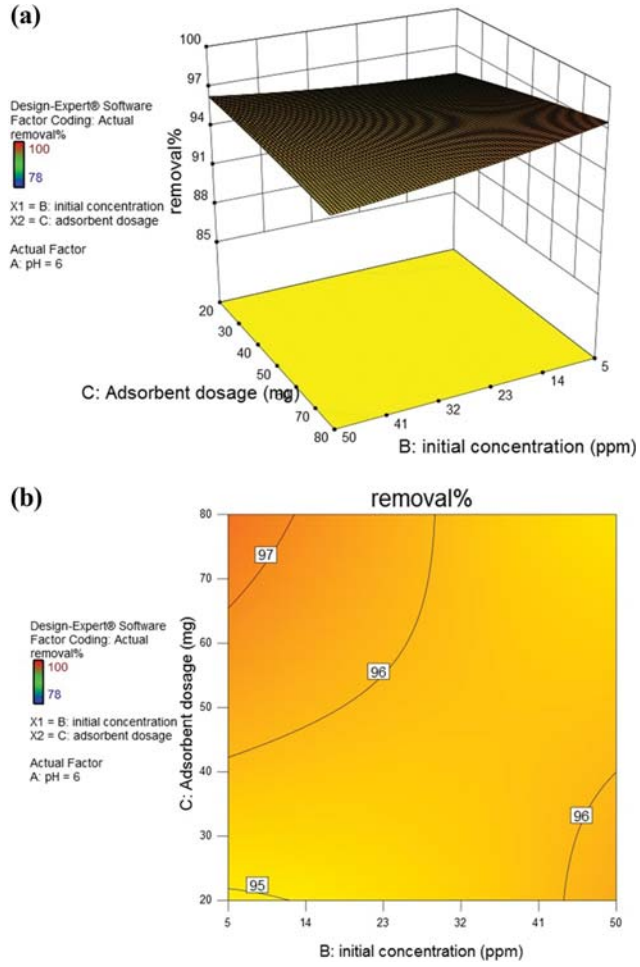

Fig. 13. (a) 3-D response surface plot and (b) contour plot showing the interaction effect of adsorbent dosage and initial pollutant concentration on Cu (II) removal using MMT-Al_2O_3 nanocomposite.

and $\log q_e$ vs. $\log C_e$, respectively which confirms that the adsorption obeys the Langmuir model. Moreover, to find the most appropriate model, the data were fitted with both isotherms and results reveal that the Langmuir model is the fittest with a correlation coefficient of R^2=0.9942 (Table 5).

Isotherm calculations show that the as-prepared nanocomposite follows Langmuir isotherm, which means ion exchange controls the mechanism of adsorption of Cu (II) ions on MMT-Al_2O_3 nanocomposite.

Table 5. Isotherm parameters for Cu (II) removal using MMT-Al_2O_3 nanocomposite

Freundlich model			Langmuir model			
n	K_f	R^2	q_m	K_L	R^2	R_L
2.29	9.82	0.9448	35.2	0.54	0.9942	0.156

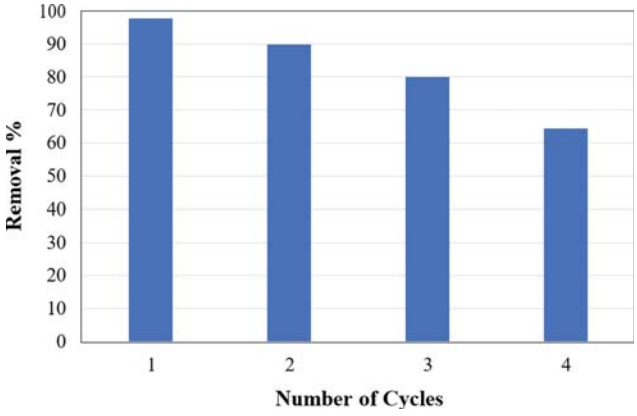

Fig. 15. Cu (II) removal from aqueous solution using MMT-Al_2O_3 during four cycles.

4. Investigation of MMT-Al_2O_3 Performance in Consecutive Cycles

The as-prepared nanocomposite performance during consecutive cycles is represented in Fig. 15. Typically, the nanocomposite is subjected to removal experiments without any reclamation. It is clear that Cu (II) removal% from aqueous solution in the first cycle is ~97.58% and this amount slightly decreased to 64.29% in the fourth cycle. It can be concluded that MMT-Al_2O_3 shows an acceptable removal up to three cycles and reclamation process is necessary for further usage.

5. RSM Modeling for MMT-Al_2O_3-Fe_3O_4 Nanocomposite

MMT-Al_2O_3-Fe_3O_4 is used for Cu (II) removal. Experiments were designed via RSM technique and the effects of solution pH (A), concentration (ppm) (B), adsorbent dose (mg) (C), contact time (D) and temperature (E) were investigated. Experimental and predicted values of Cu (II) removal using D-optimal experimental design and RSM technique are summarized in Table 6.

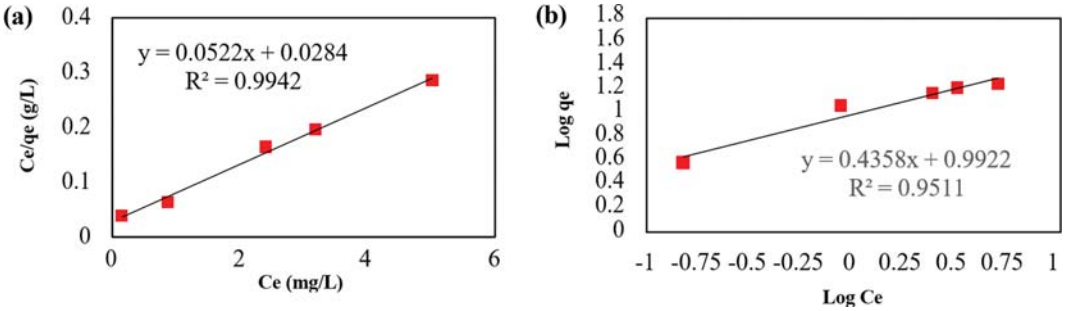

Fig. 14. (a) Langmuir and (b) Freundlich isotherms for Cu (II) removal using MMT-Al_2O_3.

Table 6. D-optimal experiment with actual and predicted response values

No.	pH (A)	Concentration (ppm) (B)	Adsorbent dose (mg) (C)	Contact time (D)	Temperature (E)	Removal (%)	
						Actual	Predicted
1	3	5	20	5	60	97.10	97.11
2	11	5	20	5	25	60.00	59.89
3	11	5	80	5	60	90.00	90.02
4	3	120	80	5	60	78.70	78.67
5	11	60	20	90	45	95.30	95.40
6	9	60	60	30	45	94.20	94.16
7	7	60	40	5	25	75.00	75.23
8	7	120	80	60	45	93.90	93.96
9	7	50	80	120	25	96.70	96.66
10	7	30	20	60	60	94.30	94.3
11	3	5	80	5	25	82.00	81.97
12	3	90	60	30	35	86.20	86.25
13	11	5	60	120	35	97.00	97.11
14	3	5	80	120	60	96.70	96.74
15	11	120	40	60	60	95.40	95.34
16	11	60	80	60	25	92.00	91.93
17	11	120	80	5	25	83.50	83.49
18	3	120	20	120	60	79.90	79.99
19	3	120	20	5	25	71.00	70.90
20	5	60	40	120	45	96.30	96.02
21	3	120	80	120	25	87.00	87.03
22	11	120	80	120	60	98.00	98.01
23	11	120	20	120	25	95.00	94.99
24	3	5	20	120	25	85.00	85.05
25	11	90	20	5	45	87.40	87.44
26	11	5	20	120	60	91.40	91.37

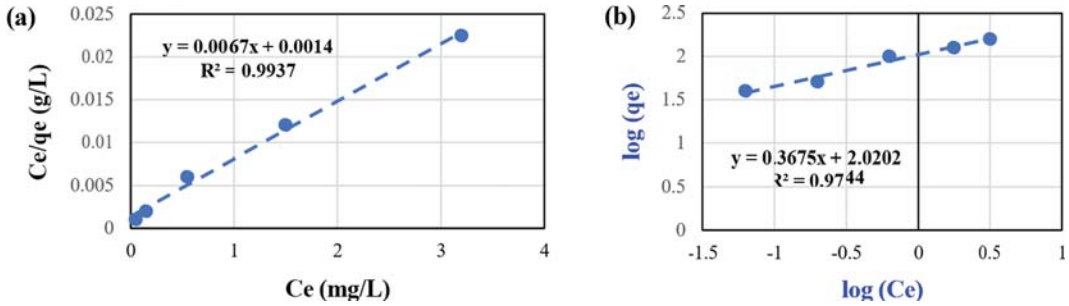

Fig. 16. (a) Langmuir and (b) Freundlich isotherms for Cu (II) removal using MMT-Al_2O_3-Fe_3O_4.

A quadratic equation is successfully fitted to the obtained removal data as follows:

$$\%\ \text{Removal} = +95.88 + 1.66\times A - 0.94\times B + 2.66\times C + 4.81\times D + 3.92\times E + 4.60\times AB + 1.24\times AC + 2.29\times AD + 0.47\times AE - 1.62\times BC - 0.21\times BD - 2.62\times BE + 0.65\times CD - 2.06\times CE - 3.54\times DE - 0.73\times A^2 - 1.38\times B^2 - 0.58\times C^2 - 1.71\times D^2 - 5.13\times E^2 \quad (8)$$

Removal experiments were repeated to evaluate MMT-Al_2O_3-Fe_3O_4 nanocomposite and comparison with MMT-Al_2O_3. It was observed that the addition of Fe_3O_4 nanoparticles resulted in the reduction of the required adsorbent dose from an initial amount of 77 mg at pH=8.3 to 26 mg at pH=11 for Cu (II) removal from the solution with an initial concentration of 36 ppm up to 120 ppm.

5-1. Adsorption Isotherm for MMT-Al_2O_3-Fe_3O_4

Figs. 16(a) and (b) reveal a linear plot of specific adsorption (C_e/q_e) as a function of equilibrium concentration C_e and $\log q_e$ vs. $\log C_e$, respectively for the MMT-Al_2O_3-Fe_3O_4 nanocomposite. Moreover, to find the most appropriate model, data were fitted with Langmuir and Freundlich isotherms (Eqs. (4)-(6)), which revealed that the Langmuir model was the fittest with a correlation coefficient

Table 7. Isotherm parameters for Cu (II) removal using MMT-Al_2O_3-Fe_3O_4 nanocomposite

Freundlich model			Langmuir model			
n	K_f	R^2	q_m	K_L	R^2	R_L
3.67	104.23	0.9754	104.92	4.31	0.9937	0.23

of R^2=0.9937 (Table 7). This confirmed that the adsorption was single layer and adsorbed Cu (II) ions were distributed evenly on the nanocomposite surface.

Isotherm calculations show that the as-prepared nanocomposite follows Langmuir isotherm which means ion exchange control the mechanism of adsorption of Cu (II) ions on MMT-Al_2O_3-Fe_3O_4 nanocomposite.

CONCLUSION

Clay mineral as a promising adsorbent not only due to containing several active sites but also an eco-friendly and cost-effective nature was used for Cu (II) removal from aqueous solutions. MMT was intercalated with Al_2O_3 nanoparticles to remove Cu (II) ions as pollutant. Furthermore, facile and cost-effective separation of the as-prepared nanocomposite from the solution upon removal was achieved through addition of Fe_3O_4 nanoparticles to MMT surface. Based on the results, in an optimal condition of pH=8.3, pollutant concentration=36 ppm and adsorbent content=77 mg, ~99% Cu (II) removal was achieved. The experimental data are well consistent with Langmuir adsorption isotherm. To investigate the adsorbent efficiency in continuous cycles, the adsorbent was utilized in five cycles without washing, indicating an acceptable removal percentage without significant reduction. Based on the results obtained in this study, clay has been proven as a promising adsorbent for heavy metals removal. The future perspective can be focused on the modification of clay with other metal oxides or other functional groups for the removal of other heavy metals. Efforts can be concentrated on the design of a nanocomposite that can be used to remove a significant range of heavy metals present in most industrial wastewaters by a combination of metal oxides and functional groups.

REFERENCES

1. M. Halim, P. Conte and A. Piccolo, *Chemosphere*, **52**, 265 (2003).
2. M. Edelstein and M. Ben-Hur, *Scientia Horticulturae*, **234**, 431 (2018).
3. K. Nalwa, A. Thakur and N. Sharma, *Advanced Materials Proceedings*, **2**, 697 (2017).
4. Guidelines for drinking-water quality, World Health Organization, 4th Ed. (2011).
5. H. A. Sani, M. B. Ahmad, M. Z. Hussein, N. A. Ibrahim, A. Musa and T. A. Saleh, *Process Saf. Environ. Prot.*, **109**, 97 (2017).
6. M. K. Uddin, *Chem. Eng. J.*, **308**, 438 (2017).
7. M. Sciban, M. Klasnja and B. Skrbic, *Wood Sci. Technol.*, **40**, 217 (2006).
8. A. Kara, L. Uzun, N. Beşirli and A. Denizli, *J. Hazard. Mater.*, **106**, 93 (2004).
9. A. Aklil, M. Mouflih and S. Sebti, *J. Hazard. Mater.*, **112**, 183 (2004).
10. M. Yusuf, F. Elfghi, S. A. Zaidi, E. Abdullah and M. A. Khan, *RSC Adv.*, **5**, 50392 (2015).
11. S. Mohan and R. Gandhimathi, *J. Hazard. Mater.*, **169**, 351 (2009).
12. A. K. Meena, G. Mishra, P. Rai, C. Rajagopal and P. Nagar, *J. Hazard. Mater.*, **122**, 161 (2005).
13. A. R. Lucaci, D. Bulgariu, M. C. Popescu and L. Bulgariu, *Water*, **12**, 372 (2020).
14. S. S. Gupta and K. G. Bhattacharyya, *J. Colloid Interface Sci.*, **295**, 21 (2006).
15. G. Zhao, X. Wu, X. Tan and X. Wang, *Open Colloid Sci. J.*, **4**, 19 (2010).
16. K. G. Bhattacharyya and S. S. Gupta, *Adv. Colloid Interface Sci.*, **140**, 114 (2008).
17. K. G. Bhattacharyya and S. S. Gupta, *Sep. Purif. Technol.*, **50**, 388 (2006).
18. S. S. Gupta and K. G. Bhattacharyya, *J. Hazard. Mater.*, **128**, 247 (2006).
19. N. Vdović, I. Jurina, S. D. Škapin and I. Sondi, *Appl. Clay Sci.*, **48**, 575 (2010).
20. A. Caneschi, D. Gatteschi, C. Sangregorio, M. Vaz, U. Costantino, M. Nocchetti and R. Vivani, *Inorg. Chim. Acta*, **338**, 127 (2002).
21. H. Jobstmann and B. Singh, *Water, Air, and Soil Pollut.*, **131**, 203 (2001).
22. A. B. Đukić, K. R. Kumrić, N. S. Vukelić, M. S. Dimitrijević, Z. D. Baščarević, S. V. Kurko and L. L. Matović, *Appl. Clay Sci.*, **103**, 20 (2015).
23. E. Eren, A. Tabak and B. Eren, *Desalination*, **257**, 163 (2010).
24. F. Almomani, R. Bhosale, M. Khraisheh and T. Almomani, *Appl. Surf. Sci.*, **506**, 144924 (2020).
25. A. Masjedi, E. Askarizadeh and S. Baniyaghoob, *Mater. Chem. Phys.*, **249**, 122917 (2020).
26. C. Su, *J. Hazard. Mater.*, **322**, 48 (2017).
27. S. F. Soares, T. Fernandes, T. Trindade and A. L. Daniel-da-Silva, *Environ. Chem. Letters*, **18**, 151 (2020).
28. A. Ainurofiq, I. Nurcahyo and R. Yulianto, *Int. J. Pharmacy Pharmaceut. Sci.*, **6**, 131 (2014).
29. K. Parida, A. C. Pradhan, J. Das and N. Sahu, *Mater. Chem. Phys.*, **113**, 244 (2009).
30. M. S. Selim, L. P. Cunningham, R. Srivastava and J. Olson, Int. Congress Advances Nonimpact Printing Tech. (1995).
31. S. K. Behera, H. Meena, S. Chakraborty and B. Meikap, *Int. J. Mining Sci. Technol.*, **28**, 621 (2018).
32. F. G. R. Filho, T. J. A. Mélo, M. S. Rabello and S. M. Silva, *Polym. Degrad. Stabil.*, **89**, 383 (2005).
33. A. K. Patra, A. Dutta and A. Bhaumik, *J. Hazard. Mater.*, **201**, 170 (2012).
34. H. Li, L. Zhang, H. Dai and H. He, *Inorg. Chem.*, **48**, 4421 (2009).
35. A. Ruíz-Baltazar, R. Esparza, G. Rosas and R. Pérez, *J. Nanomater.*, **2015**, 1 (2015).
36. C. G. Pope, *J. Chem. Educ.*, **74**, 129 (1997).
37. K. Bukka and J. D. Miller, *Clays Clay Miner.*, **40**(1), 92 (1992).
38. X. Rong, Q. Huang, X. He, H. Chen, P. Cai and W. Liang, *Colloids Surf. B: Biointerfaces*, **64**, 49 (2008).
39. W. Xue, H. He, J. Zhu and P. Yuan, *Spectrochim. Acta Part A*, **67**,

1030 (2007).
40. G. L. Teoh, K. Y. Liew and W. A. K. Mahmood, *J. Sol-Gel Sci. Technol.*, **44**, 177 (2007).
41. V. P. Dhawale, V. Khobragade and S. D. Kulkarni, *Int. J. Environ. Chem.*, **2**(1), 10 (2018).
42. G. Li, Y. Jiang, K. Huang, P. Ding and J. Chen, *J. Alloys Compd.*, **466**, 451 (2008).
43. K. Yang, H. Peng, Y. Wen and N. Li, *Appl. Surf. Sci.*, **256**, 3093 (2010).
44. L. Perassi and L. Borgnino, *Geoderma*, **232**, 600 (2014).
45. J. L. Bishop and E. Murad, *J. Raman Spectrosc.*, **35**(6), 480 (2004).
46. R. L. Frost and L. Rintoul, *Appl. Clay Sci.*, **11**(2-4), 171 (1996).
47. D. D. Wynn-Williams and H. G. M. Edwards, *Icarus*, **144**(2), 486 (2000).
48. Y. Liu, B. Cheng, K. K. Wang, G. P. Ling, J. Cai, C. L. Song and G. R. Han, *Solid State Commun.*, **178**, 16 (2014).
49. M. Gao, W. Li, J. Dong, Z. Zhang and B. Yang, *World J. Condensed Matter Physics*, **1**(2), 49 (2011).
50. B. Sohn and R. Cohen, *Chem. Mater.*, **9**, 264 (1997).
51. S. Foorginezhad and M. M. Zerafat, *Ceram. Int.*, **43**, 15146 (2017).
52. M. Arabi, M. Ghaedi, A., Ostovan, J. Tashkhourian and H. Asadallahzadeh, *Ultrason. Sonochem.*, **33**, 67 (2016).
53. Y. Abdellaoui, M. T. Olguín, M. Abatal, B. Ali, S. E. D. Méndez and A. A. Santiago, *Superlat. Microstruc.*, **127**, 165 (2019).
54. M. B. Desta, *J. Thermodyn.*, **2013**, 64 (2013).
55. B. Hameed, A. M. Din and A. Ahmad, *J. Hazard. Mater.*, **141**, 819 (2007).